Materials & Design 212 (2021) 110199

Contents lists available at ScienceDirect

Materials & Design

journal homepage: www.elsevier.com/locate/matdes

Ablation behaviour of carbon fibre ultra-high temperature composites at oblique angles of attack

B. Baker [a,*], V. Venkatachalam [a], L. Zoli [b], A. Vinci [b], S. Failla [b], D. Sciti [b], J. Binner [a]

[a] School of Metallurgy and Materials, University of Birmingham, Edgbaston, Birmingham, UK
[b] CNR-ISTEC, Institute of Science and Technology for Ceramics, Via Granarolo, 64 - 48018 Faenza, Italy

HIGHLIGHTS

- Angled torch testing of ceramic composites at 90-10° doubled surface shear stress.
- Low angles reduced incident surface pressure by ~85%.
- Surface temperatures decreased by 15% at reduced incident angles.
- Damage area and oxide microstructure reduced commensurately with temperature.
- The aerodynamic flow regime modified oxidation behaviour significantly

GRAPHICAL ABSTRACT

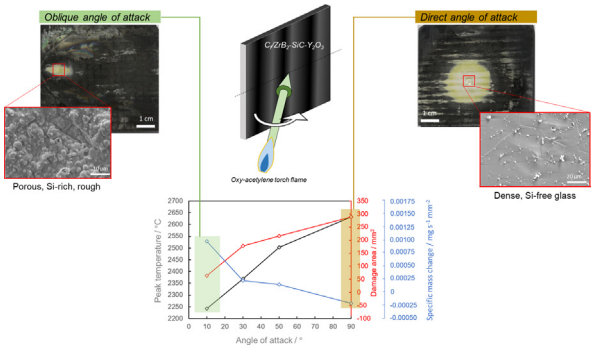

ARTICLE INFO

Article history:
Received 27 June 2021
Revised 12 October 2021
Accepted 26 October 2021
Available online 27 October 2021

Keywords:
Oxyacetylene torch testing
Ablation analysis
Ultra-high temperature ceramics
Ceramic matrix composites
Oxidation test methods

ABSTRACT

Oxyacetylene torch testing was performed at a range of angles of attack on C_f/ZrB_2-SiC-Y_2O_3 composites, from 10° to 90°. The ablation behaviour was studied *in-situ* with thermography, and the post-ablation morphologies investigated optically and with elemental analysis. Significantly lower surface temperatures were observed at oblique angles of attack leading to less damage in terms of both oxidation extent and material removal. Rudimentary modelling of a gas stream impinging on a perfect surface showed that the angular variation also led to a significant drop in pressure at more oblique angles of attack, with a commensurate increase in shear stress. The surface oxide formed during testing seemed mainly to correspond to the temperature distribution and was apparently more susceptible to damage from higher impinging pressure than shear stress. This study elucidated some interesting aspects of a modified ablation test and showed some new parameter ranges which may be useful in targeted material screening.

1. Introduction

Ultra-high temperature ceramic matrix composites, UHTCMCs, are promising candidate materials for use in rocket engines and for sharp leading edges of hypersonic control surfaces. They are exposed to significant thermomechanical loads and corrosive atmospheres during use [1,2]. Optimising the materials to produce components that are dimensionally stable during the oxidation inherent to the application conditions, and that are resistive to ablation and spalling, is a key development area to move towards commercialisation [3]. UHTCs, whilst possessing high strength and thermal conductivity [4–6], oxidise at reasonably low temperatures in high pO_2 environments [7]. In the case of ZrC and HfC, two commonly investigated UHTCs, this is accompanied by an evolution of CO_x gases [8,9]. The expansion of these gases upon generation can result in open channels leading to enhanced oxygen ingress to the body of the component [8]. The formation of the

* Corresponding author.
E-mail address: benabaker94@gmail.com (B. Baker).

https://doi.org/10.1016/j.matdes.2021.110199
0264-1275/

$(Zr/Hf)O_2$ product can also produce a non-protective porous solid scale, with linear oxidation kinetics seen at temperatures below the melting point of the oxide products [7]. Above this temperature, the fluid melt can act as an oxygen-passivating barrier layer. However, in a scouring gas environment, the mechanical stability of this fluid may be limited and its removal can result in further oxidation of the component leading to catastrophic failure [10]. For the boride UHTCs, ZrB_2 and HfB_2, oxidation proceeds via a liquid B_2O_3 intermediate at temperatures below 1000 °C [11], which likewise acts as a passivating fluid scale [12]. When integrated to the solid $(Zr/Hf)O_2$ network this adds a certain resistance to aerodynamic denudation . However, at temperatures beyond the vaporisation temperature of B_2O_3, this mechanism of protection is lost and the components are again vulnerable to oxidation [13].

A proposed method of enhancing the temperature range of these components is in the doping of materials to improve the thermodynamic and mechanical longevity of the passivating liquid–solid hybrid oxide scale [14–16]. There are various explanations of this effect, which involve enhancement of fluid viscosity, wettability and reduction in the vapour pressure. Some researchers have found success in improving the ablation resistance by addition of SiC in the temperature range < 1650 °C [17–19], or further modifications involving combinations of other oxides (e.g. Ta) up to a reported 2900 °C [20,21]. Recently Sciti et al. reported the addition of 5 vol% of Y_2O_3 to further decrease the porosity of C_f/ZrB_2-SiC materials via due to the formation of a liquid phase with the oxide impurities present on the surface of ZrB_2 and SiC grains [22].

Oxyacetylene-torch ('OAT') testing is a cheap and rapid screening method for UHTCMC samples [23–26]. It provides incredibly high heat fluxes of up to around 20 MW m^{-2} in oxidising environments [27] and is significantly easier, faster and cheaper to perform than stagnation pressure tests, arc-jet tests or plasma tunnel tests, though the latter do provide a more holistic representation of the chemothermomechanical environment of interest [28]. However, an area where OAT testing significantly misrepresents the application conditions is the gas speed (and therefore stagnation pressure) incident on the sample, which has been estimated to be around Mach 0.6 [27]. Whilst the samples are heated to the desired temperature and the formation of the expected oxidation products occurs, the coupling of these aspects with a far lower flow speed ensure that the success or failure of the composition being screened is only truly representative of the reduced flow environment. A potential issue is that the relatively mild mechanical regime (when compared to more energy-intensive test methods or the application conditions) permits protection mechanisms to occur that would not be effective in more aggressive conditions, such as the re-entry environment for example. Whilst the OAT test is only ever intended to provide a rough guide to materials selection, its lack of high-speed gas flow can mean that some materials that progress to subsequent stages of testing are found to be unsuitable. For instance, Ni et al. [29] found the formation of uncommon microstructures of SiO_2 – root-like growths and wires – on the ablation testing of SiC coated C/C composite apertures at 0° angle of attack at heating levels capable of heating the surface to almost 2000 °C – far above the melting temperature of SiO_2. Application of multiple OAT oxidation cycles of C/C-ZrC-SiC-ZrB_2 composites by Zhao et al [30], four 30 s segments versus two 60 s, resulted in greater surface damage for the four segmented heating profile, thus showing the importance of controlling the frequency and magnitude of the surface expansion on heating on the oxidation performance of UHTC composites. However, the purposeful probing of the shearing aerodynamic forces and distribution of heat flux gradients across a surface provided by angular OAT testing have not been reported until now.

This paper seeks to investigate a simple modification of the OAT method to help probe different aerothermal regimes. It is possible that by modifying the angle of attack (whilst retaining the same heat flux), the force will become distributed between both compressive and shearing modes at the sample surface [31]. Increased shearing modes will affect, and possibly displace, the materials most weakly bonded to the surface. These will inevitably be the adherent oxide scales responsible for oxidation protection. Hence, by manipulating the gas flow, removal of potentially protective material may result in material failure. It is hoped that by probing these effects, artefacts of the test method and ramifications concerning perceived material performance may become easier to identify, in what is nominally the same test environment, as the angle is usually a factor ignored in the literature. Secondly, materials situated in a less-aggressive, more oblique angle of attack, region of components such as aerospace vehicle skins or exhaust channels, such as those studied by Sciti et al [32] in another article recently published in this journal, will benefit in a screening method which provides gas flow characteristics more like in-situ conditions. Development and validation of such a test environment would allow faster, more efficient, and a more iterative approach to materials design for such components. The simplicity of the modifications in this study are accessible to any facility with access to an OAT, therefore the results of this method and the potential benefits for the material design process they bring are accessible to all relevant people in the research community.

2. Materials and methods

2.1. Sample production

The samples studied in this work were provided by CNR-ISTEC and were obtained by slurry infiltration and sintering. Unlike conventional bulk ceramics for which a wide array of known processing techniques is available, the processing of UHTCMCs is complicated by the presence of the fibre reinforcement. Powder mixtures are prepared by wet ball milling of the starting powders with SiC grinding media in absolute ethanol (water content < 0.05%) for 24 h at 60 rpm. Commercially available powders were used for the preparation of the ceramic composite materials: ZrB_2 (H.C. Starck, grade B, Germany) and α-SiC (H.C. Starck, Grade UF-25, Germany), Y_2O_3 (Starck, Germany), carbon fibres (pitch fibres XN80, NGF, Japan). After ball milling, the powders were completely dried with a rotary evaporator at 90 °C and then sieved. With these powders, aqueous suspensions (the exact composition is proprietary) were prepared following the procedures described by Zoli and Vinci et al. [22,33] in a 90:7:3 ZrB_2:SiC:Y_2O_3 weight ratio, the fibre preforms were infiltrated by slurry infiltration and the layers stacked in a 0/90° configuration. The green pellet was cut in a graphite die and consolidated via hot pressing, initially under vacuum at 1900 °C and then under a uni-axial pressure of 30 MPa for 15 min.

2.2. Oxyacetylene torch testing

Oxyacetylene torch testing was performed with a bespoke facility at the University of Birmingham. Flow rates of 0.8 m^3 $hour^{-1}$ for acetylene and 1.1 m^3 $hour^{-1}$ were used, obtaining a heat flux of 17 MW m^{-2} for testing at 10 mm distance, with gas speeds of around Mach 0.6. Details concerning the calculation of the heat-flux provided by this specific torch facility may be found in a separate publication [27]. The samples were fixed in a water-cooled graphite sample holder and rotated directly into the flame to begin the test. A video of a typical test has been submitted in the Supplementary Materials for reference. The front face temperature was

measured by both a 2-colour pyrometer (Metis M3, SensorTherm GmbH, Sulzbach, Germany) and an infrared camera (A655sc, FLIR, Wilsonville OR, USA). The rear face temperature was measured with a k-type thermocouple. An image of the facility permitting angled testing is included in Fig. 1.

The thermal gradient was investigated using the IR thermal imaging data with ResearchIR (FLIR Systems). This was calibrated with regards to emissivity using the 2-colour pyrometer data. The thermal gradient was compared to the surface damage and phase change distribution, in addition to the hydrodynamic regime inferred from simulations, to confirm the effect of the changing test environment on the sample behaviour. The pyrometer's optical filter allowed viewing of the evolution of the surface morphology.

2.3. Surface and microstructural analysis

Samples were characterised by mass change rate over the regions of interest. The surface phase microstructure was mapped using scanning electron microscopy (SEM, Jeol 7000, Tokyo, Japan) and electron dispersive spectroscopy (EDS, Oxford Instruments, Oxford, UK). Surface profilimetry was performed to correlate against the thermal gradient (InfiniteFocus, Alicona Imaging GmbH, Graz, Austria). Image analysis was performed (ImageJ, National Institute of Health, MA, USA) to calculate the surface oxidation area after appropriate scaling and to compare to the thermograms measured during the test. Images were 'colour thresholded' such that the oxidised areas were included in pixel counting. This was performed manually, with the colour channels selected for each image.

Mass change rate ($\Delta m/\Delta t$) was determined by:

$$\frac{\Delta m}{\Delta t} = \frac{m_{final} - m_{initial}}{\Delta t}$$

120 s was the test duration in all cases in this work, excluding for a trial sample at 10° tested for 60 s. This sample was removed from the analysis, as mass change over time in an oxidation test can be expected to vary non-linearly with time. A positive $\Delta m/\Delta t$ indicates a net mass gain over the duration of the test, due to the formation of oxidation products with a higher mass than the initial sample. A negative value means a net mass loss over the test, indicating loss of material due to ablation or gaseous evolution.

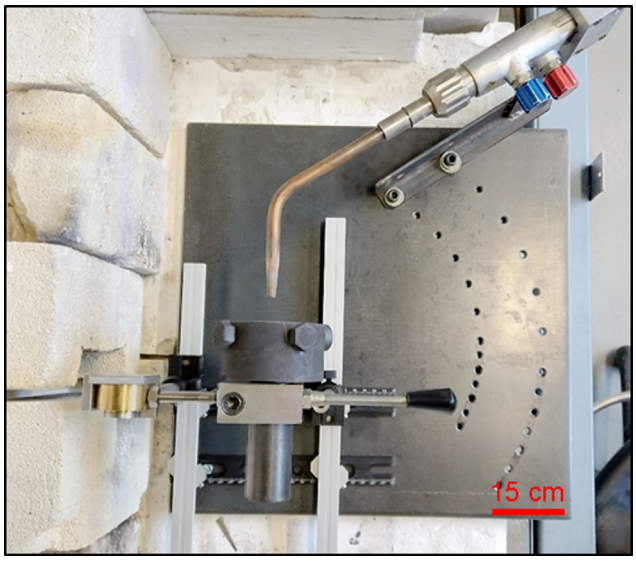

Fig. 1. Plan image of variable angle torch test rig. The angle and sample x-y coordinate centre may be varied using the array of drilled holes to ensure precise angle and test distances.

Specific $\Delta m/\Delta t$ is the mass change rate calculated divided by the area of the oxidised region.

The oxide scales' crystal structure and phases were examined using X-ray diffraction (XRD, Bruker D8, Coventry UK) and Raman spectroscopy (inVia Reflex, Reinshaw, New Mills, U.K).

2.4. Numerical simulations

The working fluid properties used were that of air at room temperature. The surface pressure and wall shear were analysed across the sample surface.

Numerical simulations were performed in ANSYS Fluent (ANSYS, PA, USA). A schematic diagram in 2 dimensions of the geometry for the 50° angle of attack is shown in Fig. 2. A 3D view of the simulation space is shown in Fig. 3. An unstructured grid consisting of tetrahedral elements was used. The mesh generation algorithm was retained for all tests and a standard simulation divided the solution area into between 800,000 and 1,000,000 elements.

A finite volume method was used for the solution of the Navier-Stokes equations. A coupled scheme was used for the pressure and velocity, and the PRESTO! scheme was used for pressure discretisation. A second order upwind scheme was used for the momentum calculation, whereas a first order upwind scheme was used for the formulation of the k-ε turbulence equations (standard). Turbulence was expected for the Reynolds number of this flow (~30,000 for air at 298 K in the geometry shown).

The wall shear was determined by:

$$\tau_W = \mu \frac{\partial u}{\partial n}$$

where μ is the dynamic viscosity of the fluid and the partial differential is the velocity gradient in the fluid adjacent to the no-slip defined wall, i.e. the sample surface in Fig. 3. The grid resolution at the surface was important for resolving this gradient and a face sizing scheme was imposed here to ensure sufficient detail capture.

The wall pressure was determined from the local flow field details.

3. Results

3.1. Sample summary

The samples that were produced as outlined above conformed to the general volume percentage ratios of 35 vol% C_f (0/90° orientation), 65 vol% matrix (90% ZrB_2 + 7% SiC + 3% Y_2O_3). The masses and densities of the produced samples are shown in Table 1. The microstructure of the as-produced material is shown in Fig. 4.

Fibres were homogeneously distributed across the composite, with most fibres individually surrounded by a layer of ceramic matrix (Fig. 4b). SiC was found as small particles at ZrB_2 grain boundaries and occasionally as agglomerates. The latter likely originated from a non– homogeneous dispersion in the powder suspension used for slurry infiltration. The fibre/matrix interface was strong, as evidenced by the high magnification micrograph (Fig. 4c) where the outer fibre surface has partially reacted with the matrix, and from the fracture surface (Fig. 4d) showing the short extent of fibre pull-out (<20 μm). The porosity, obtained as the difference from the relative density value, amounted to less than 5 vol% due to formation of a liquid phase that aided the sintering of ZrB_2. This was accompanied by an increase of ZrB_2 grain size of about 50 % (from 2.5 to 3.7 μm). The ZrB_2 grain coarsening suggests dissolution and re-precipitation mechanisms. All these mechanisms indicate a liquid phase sintering mechanism. According to the SiO_2-Y_2O_3 phase diagram (eutectic exists at ~1650 °C) a

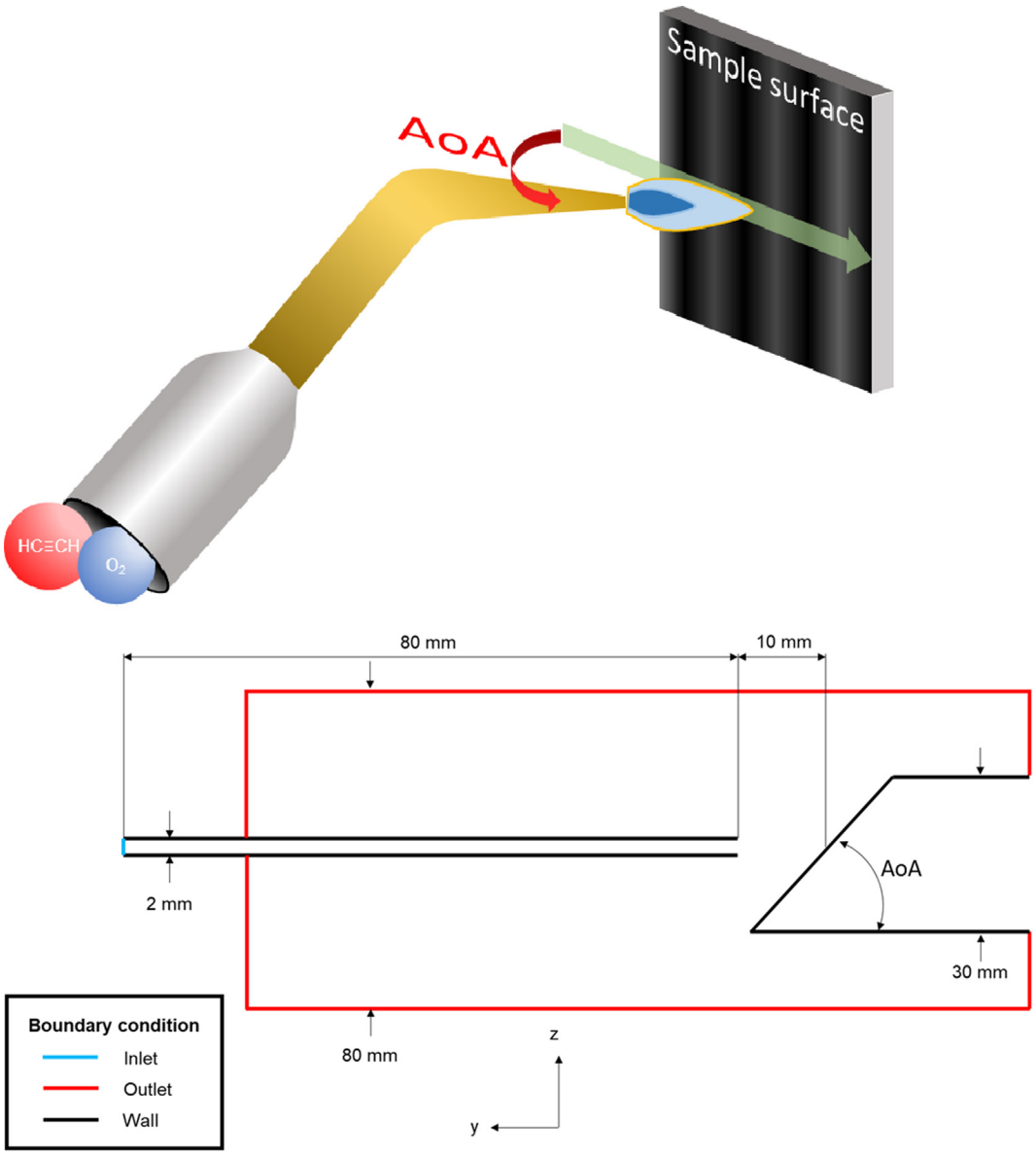

Fig. 2. A schematic in 2D of the geometry used in the flow modelling calculations, with a schematic of the features of the test being represented. Red indicates pressure outlet conditions, black indicates interior wall boundary conditions and blue indicates the velocity inlet.

liquid phase could be formed between Y_2O_3 particles and SiO_2 impurities (distributed on surface of SiC particle) [22].

3.2. Ablation analysis

The characteristic ablation patterns for each angle of attack investigated are shown in Fig. 5. The shape, size and aspect ratio of the oxidised areas changed as the angle of attack was reduced from 90° to 10°. As expected, this change was from a circular, radially symmetric oxidation morphology to a skewed ellipse.

The width, length and area of the damaged samples as determined by image analysis are shown in the Fig. 6a. The oxidised width, the dimension indicated in Fig. 5c, can be seen to increase by a greater margin than the damage length as the angle changes.

Fig. 7 shows the temperature distribution as determined by IR thermography across the indicated surface line segment. At higher angles of attack, the temperature distribution across the indicated bisecting line show that both the peak temperature increased and the temperature distribution became more symmetrical. This is matched by the obvious decrease in aspect ratio to circular at 90° compared to those at 30° and 10°.

$\Delta m/\Delta t$ is displayed in Fig. 8, with 3 different samples being tested at each angle. $\Delta m/\Delta t$ can be seen to increase slightly as the angle of attack was decreased, i.e. grazing angles were less damaging in terms of material removal than a direct, 90° angle of attack. It should be noted, however, that one of the samples tested at 90° showed significant variability in its results compared to the other two, far more than for any of the other angles. The probable reason for this was an error in distance, set at the beginning of the test. Since there was no opportunity to retest a fresh sample, this data point has been excluded from the analysis.

The peak static pressure and wall shear from the modelling results are shown in Fig. 9a. As the angle of attack increased from 10° to 90° the wall shear increased markedly, by 1.5x, whilst the surface static pressure was reduced by a far higher proportion, almost 0.1x the value at 90°. Comparing this value to the integrated value over the work surface in Fig. 9b, they can be seen to follow the same trend (though note the change in units). It is

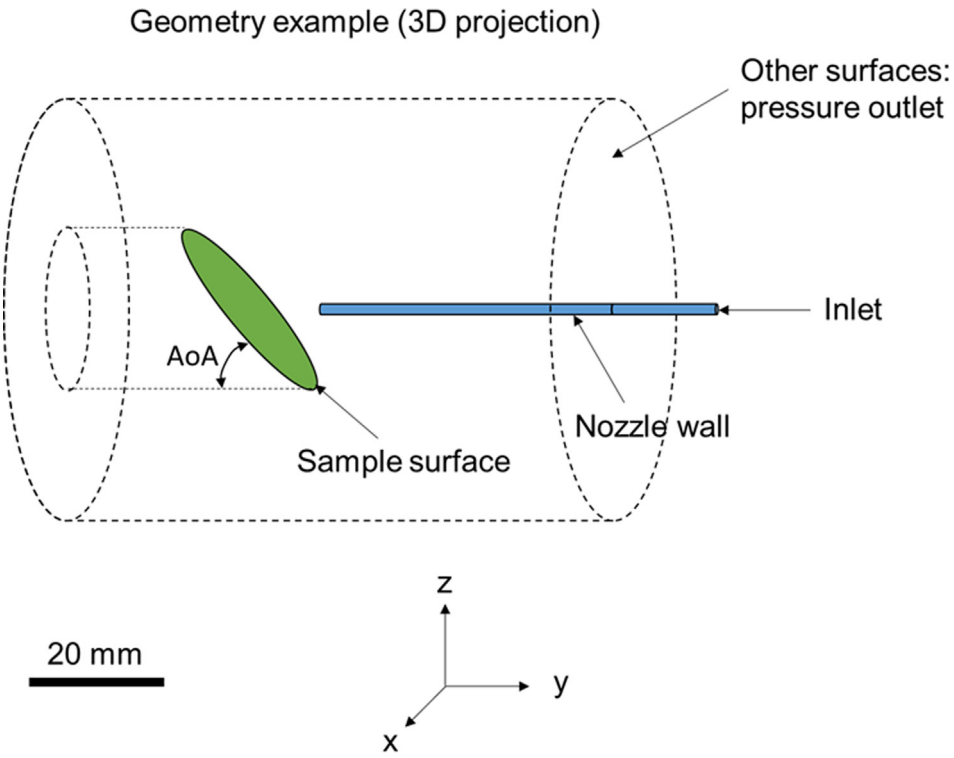

Fig. 3. A 3D representation of the geometry used in the fluid dynamics calculations.

Table 1
The specifications of the as-produced samples.

Sample #	Mass/g	Dimensions/mm			Density/g cm^{-3}	
		Width	Length	Height	Archimedes	Geometric
#1	61.7862	43.59	48.09	7.09	4.20	4.16
#2	62.369	43.55	48	7.14	4.10	4.18
#3	62.2162	43.47	47.9	7.05	4.10	4.24
#4	62.8532	43.5	48.01	7.16	4.17	4.20
#5	61.5811	46.56	48.09	7.11	4.15	3.87
#6	63.0687	43.53	47.04	7.14	4.32	4.31
#7	62.4286	43.55	47.76	7.16	4.20	4.19
#8	62.6423	43.54	47.92	7.18	4.20	4.18
#9	65.3159	43.72	47.98	7.47	4.11	4.17
#10	67.2917	43.51	48.02	8.18	3.99	3.94
#11	64.2994	43.45	48.07	8.12	3.82	3.79
#12	71.1053	43.55	47.73	8.15	4.24	4.20

important to consider the changing surface area of the analysis surface, which can be expected to vary as shown in Fig. 10. Given the concentration of large magnitudes of both static pressure and wall shear around the torch tip in all cases, however, the 'extra area' the integral is calculated over does not result in a significant increase in either variable.

XRD analysis, Fig. 11, showed that phases other than t-ZrO_2 were largely absent from the surface in the oxidised areas of the test specimens, excluding that for the 10° sample, for which there is evidence of the unreacted starting materials.

SEM imaging of the post-test samples are shown in Fig. 12. For the samples tested at 90°, a large grained microstructure resulted in the centre of the damage area, Fig. 12(a), possibly from melt-solidification. Large, ~2 μm, round pores were found in the surface, perhaps indicative of outgassing of volatile by-products, e.g. $SiO_{(g)}$ and $B_2O_{3(g)}$. Further away from this central region, Fig. 12(b), the surface shows sub-micron texturing suggesting nanograined t-ZrO_2, bound together with large pores. The central region of the 30° sample, Fig. 12(c), shows similar pore sizes as the 90° sample, but with significantly smaller zirconia grains and with significantly greater roughness. In the outer oxidised region, Fig. 12(d), fine ZrO_2 grains can be seen dispersed in a silicate glass. These morphologies are repeated in the 10° sample, Fig. 12(e) and (f), with fewer pores and larger structure sizes than in the 30° case. SEM analysis detected traces of Si in both the central and more distant regions. Fig. 13 shows that nano ZrO_2 grains were embedded in a glassy matrix. This corroborates the results from Raman spectroscopy; formation of a biphasic ZrO_2-SiO_2 network was preferred over formation of a zirconium silicate glass. Some similar behaviour was seen by Ma et al [34] in Y_2O_3 modified ZrB_2-SiC coatings after oxidation testing at 1450 °C for 10 h – a 71:5:24 ZrB_2:Y_2O_3:SiC coating produced post-oxidation phases of predominately Y_2SiO_4, t-ZrO_2 and SiO_2.

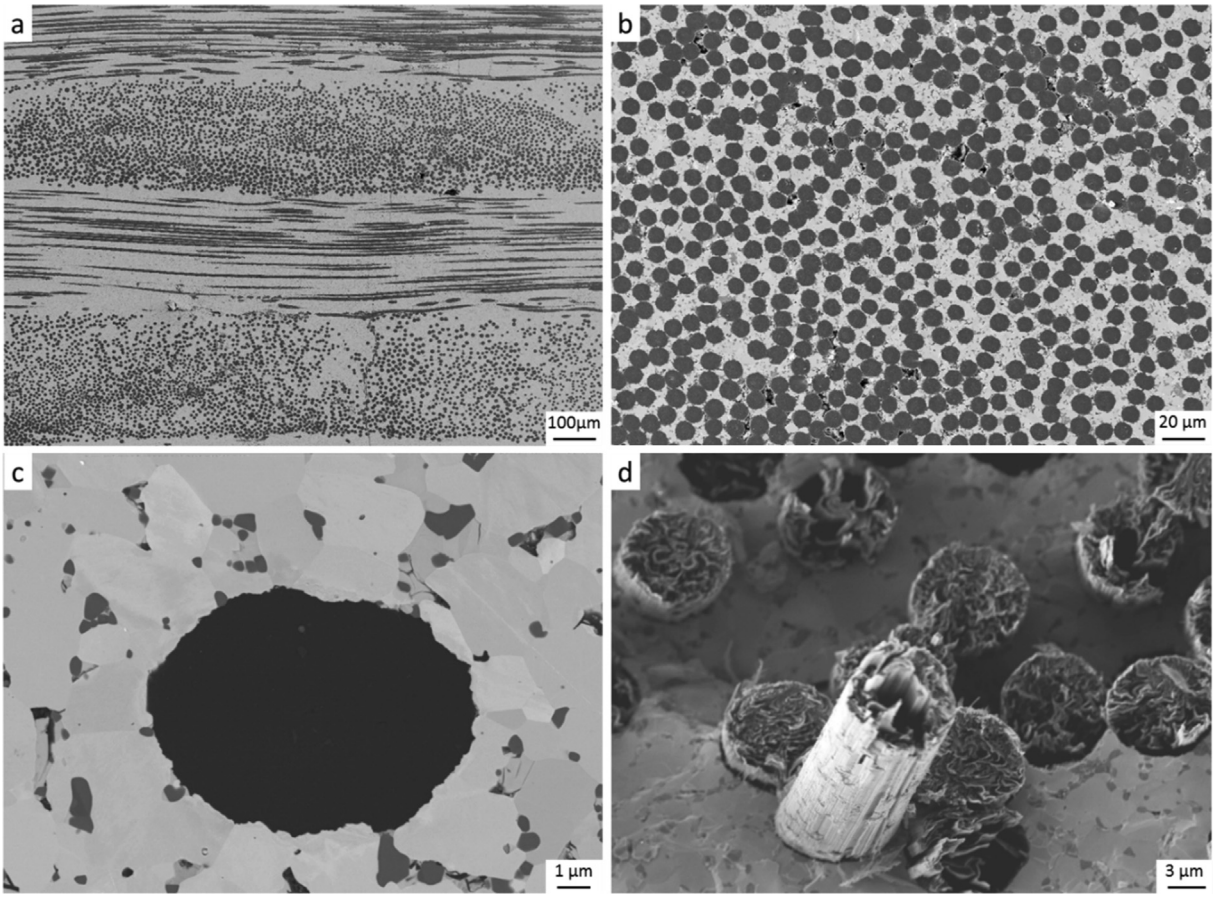

Fig. 4. Microstructure of the pristine sample: a) 0/90° layer configuration where the UHTC matrix is in white and the fibres in black, b) homogeneous fibre distribution in the matrix, c) fibre/matrix interface, d) fibre pull-out.

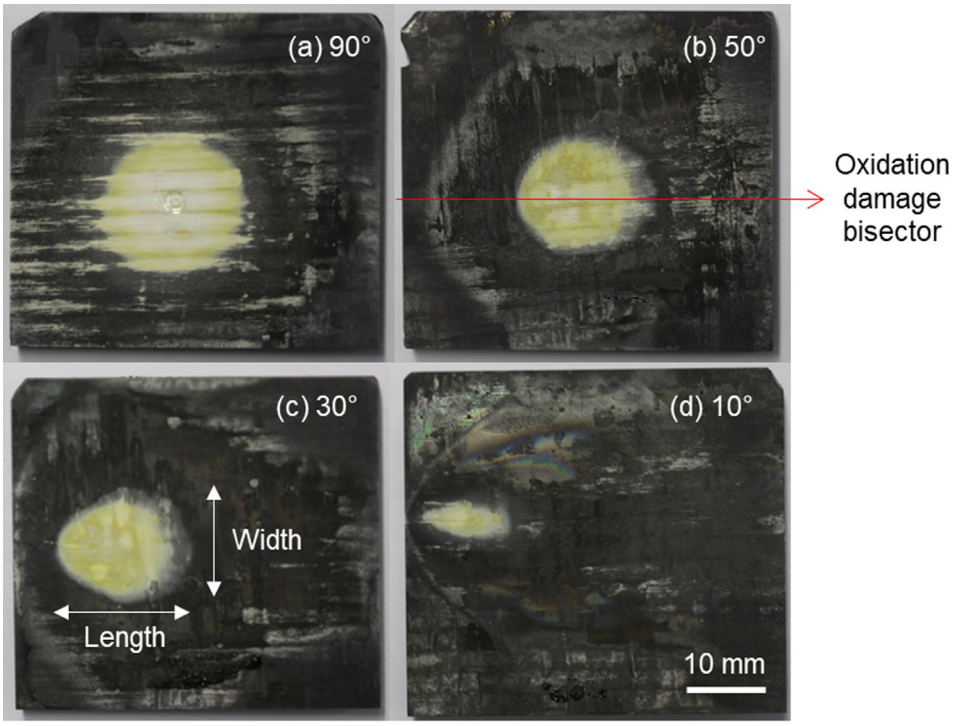

Fig. 5. The characteristic ablation morphologies post-test by angle; (a) 90°, (b) 50°, (c) 30° and (d) 10°. The total thresholded damage area and individual lengths, horizontally and vertically, of the ablation morphologies resulting from the angled torch testing are shown in Fig. 6. The indicated oxidation damage vector is the same vector on which the thermographic line scans are measured.

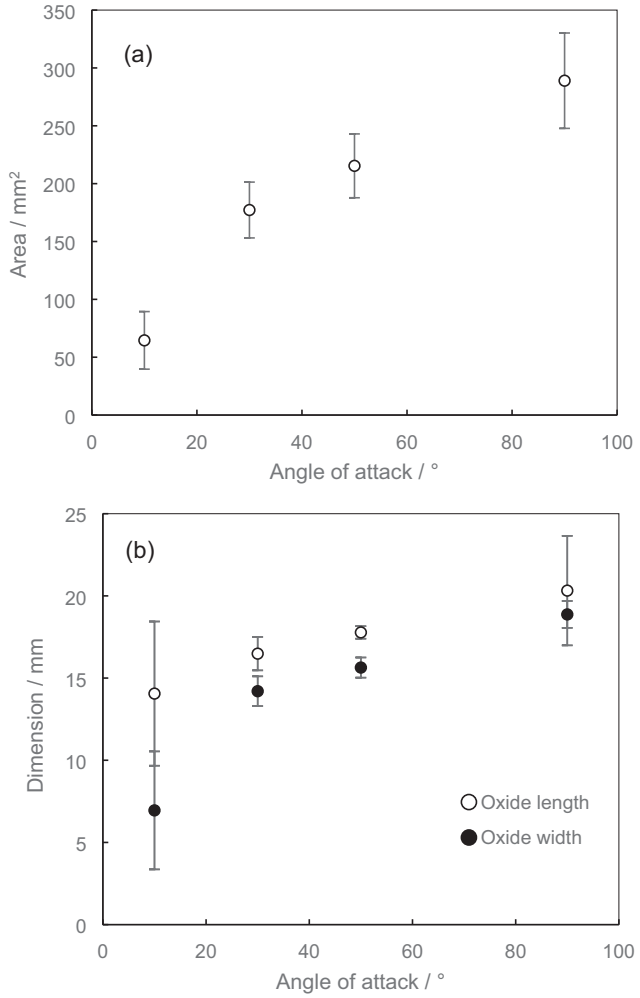

Fig. 6. (a) the total thresholded damage area and (b) individual lengths as defined in Fig. 5c of the ablation morphologies resulting from the angled torch testing.

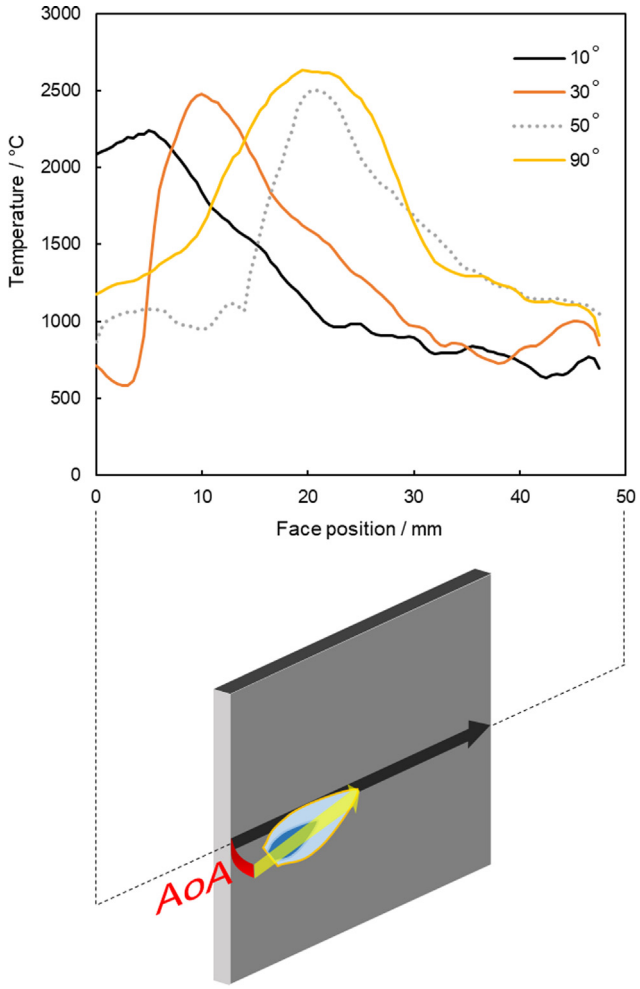

Fig. 7. The thermographic line scans of four samples taken at each incident angle condition. The line scan was collected over the bisector indicated in Fig. 5b in all cases.

4. Discussion

The heat fluxes used were determined for the equal torch conditions (0.8 m^3 h^{-1} acetylene, 1.1 m^3 h^{-1} oxygen), by this group using this same torch facility in a seperate work [27].

However, direct application of this data requires certain caveats. The tilt of the samples due to relative angle of attack will result in a distance distribution of the surface of the sample from the torch tip. Hence, not all the surface will be at the nominal 10 mm test distance; some parts will be closer and some will be farther away. Furthermore, the parts of the sample upwind of the 10 mm focus point on the sample surface will be rotated to be further way from, and further up from, the flame cone - the hot region, which has a thickness of only a few milimetres [35]. As such, the heat flux experienced in these locations, even though they are closer to the torch tip, are not likely to increase commensurately as the torch is not an isotropic heat source. Thirdly, radiative heat flux possesses an angular dependence which is in this case a further scaling factor based on test angle of cosine(90°-angle of attack) [36]. In all considerations, the heat flux of the sample surface should be expected to decrease from the nominal 1-D value of 17 MW m^{-2}. Measurement of the heat flux at different angles using a plate-like sensor, or further modelling of these features, is recommended for future work. Furthermore, the contributions of radiative, chemical (i.e. radical recombination at the surface) and conductive heat flux provided by the torch and their relative effect on surface heating of UHTC samples would aid in sample analysis.

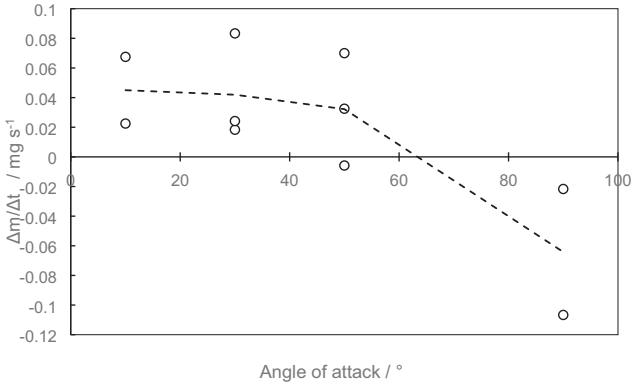

Fig. 8. Δm/Δt distribution as a function of incident angle. Three different samples were tested at each angle. The dashed line is guide for the eye passing through the set mean.

Δm/Δt shows a slight positive increase as the angle of attack is reduced and can be combined with the oxidised area to produce a specific Δm/Δt; a mass change per unit area of oxidised surface.

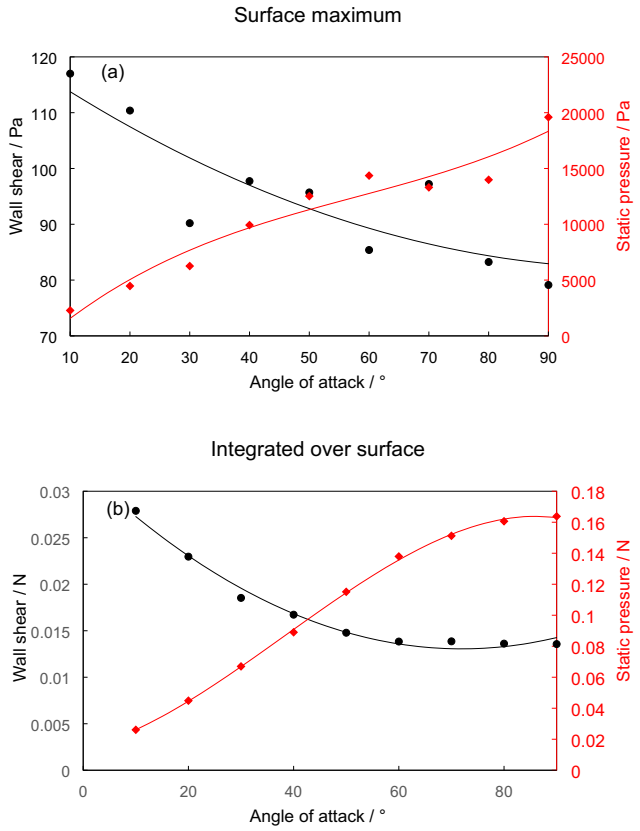

Fig. 9. The output from the fluid dynamics calculations. (a) The wall shear and pressure maxima on the sample surface; (b) the integrated wall shear and pressures over the sample surface. In either case, the trendlines are fitted by 3rd order polynomial regressions intended only as guides for the eye.

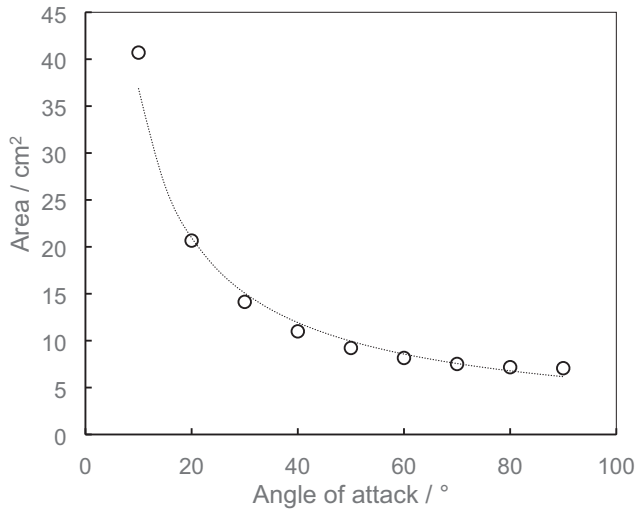

Fig. 10. The angular dependence of the sample surface area.

This is shown in Fig. 14, combined with the peak temperature (Fig. 14a), integrated pressure from the modelling (Fig. 14b) and integrated wall shear (Fig. 14c). The specific $\Delta m/\Delta t$ can be seen to correlate with the change in integrated wall shear over the sample surface. It also correlates inversely with both temperature and pressure. As the $\Delta m/\Delta t$ value is a balance between the mass gain due to the formation of the denser oxide products (when comparing to SiC and ZrB_2) and the mass loss due to their displacement from the surface and burning of carbon fibre, a positive value indicates either that more oxide is being produced, or that less material is being displaced. Fig. 6a shows that less oxide is being produced as the angle of attack is reduced. This is likely explained by the thermographic line scans indicated in Fig. 7 – much of the sample surface is of a lower temperature when the angle of attack is oblique. Hence, the larger value of $\Delta m/\Delta t$ for the oblique angles of attack must be a result of reduced material removal compared to the 90° case. This is prominent, given the reduced production of oxide. The microstructure reflects this. The porous and asperity dense surface of sintered t-ZrO_2 grains shown in Fig. 12(c–f) shows the time-stability of the non-silicate phases. However, the glassy microstructure of Fig. 12(a) shows that a liquid phase was dominant in the hot-zone of the 90° sample – such a liquid zirconia phase may be susceptible to significant mass losses due to evaporation. The vapour pressure of ZrO_2 at its melting point was calculated by Jacobson as around $2x10^{-4}$ atm [37]. Kondo et al [38] demonstrated vapour losses of up to 7 wt% resulted from the heating of molten ZrO_2 in aerodynamic levitation experiments of no longer than 1 min at around 3000 K. This value can be expected to be reduced due to yttria doping in this case. Furthermore, the low viscosity of molten ZrO_2, 13 mPa at its melting point as found by Kondo, would make the liquid phase susceptible to spallation.

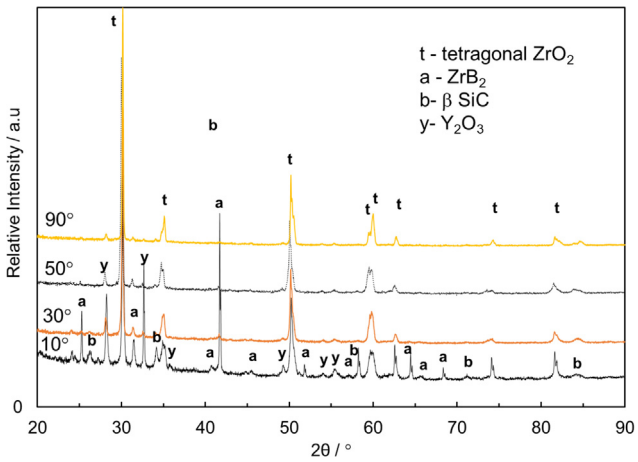

Fig. 11. The XRD diffraction patterns of the centre of the samples after ablation for 2 min.

The temperature changes can adequately explain many of the microstructural differences observed in the SEM analysis. The highest temperature regime, 90°, showed that a melt had existed that consisted of t-ZrO_2. Allowing for both the quoted error range of the pyrometer (0.5%, which is equivalent to ± 15 °C) and other factors such as the non-constant emissivity ratio between the two pyrometer channels over the course of the heating, the measured peak surface temperature of 2640 °C is close to the approximate melting point of YSZ of 2680 °C [39]. The flat surface morphology, large grain sizes and large round bubbles corroborate this observation. The shallower angles of attack, 30° and 10°, do not share this morphology, corresponding with the lower measured peak temperatures over the course of the ablation; 2370 °C and 2230 °C, respectively. The surfaces of these samples are similar: pores exist where gas may have escaped from the central region, possibly due to the active oxidation of SiC or evaporation of B_2O_3/SiO_2. This behaviour is consistent with the decreased temperature, as is the existence of the glassy phases on the periphery of the sample surfaces. At these similar distances from the 'hot zone' in the 90° sample, Si is still not detected by EDS and a fine-grained, single phase ZrO_2 region is seen.

On this basis, it is likely that the damage behaviour seen over the angle range is line with the peak temperature and distribution.

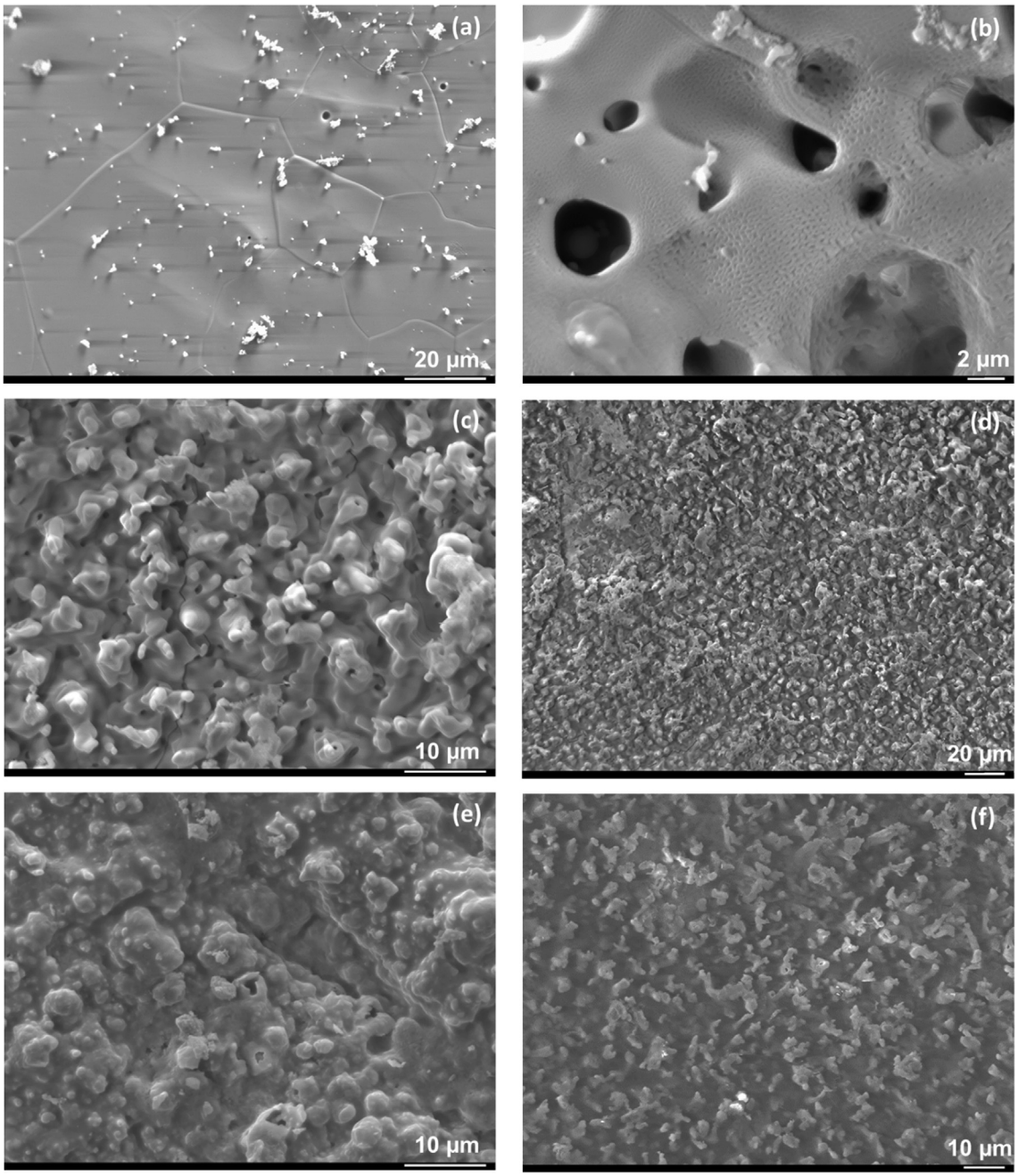

Fig. 12. SEM images of the post-ablation surface morphologies. (a, c & e) were collected at the centres of the ablated regions; (b, d & f) were collected at the extremities of the oxidised region. (a & b) were tested at 90°, (c & d) at 30° and (e & f) at 10°.

The lower temperatures may be caused by the presumed lower residence time of the hot gases at the surface, and the presumably lower heat flux incident across the surfaces. The distance travelled by the flame gas is reduced for the oblique cases compared to the 90° case. In the latter, the flame must bend through a right angle at the surface, requiring significant redirection of the gas stream and loss of momentum. In the oblique case, it does not – only a slight adjustment is required and much of the gas stream velocity can be retained. However, being directed in one direction (the plane in which the surface is tilted relative to the flame), the hot gas spreads out less in other directions and meets a lower amount of 'oxidisable' surface. The increased velocity is evidenced by the increased shear force at the surface of the sample shown in Fig. 9b at lower angles of attack. There was no indication that this increased force increased the damage on the sample surface. It is unlikely that the correlation shown in Fig. 14c, specific $\Delta m/\Delta t$ with shear force, is more than coincidental – it seems more plausible from a physical point of view for the reduced damage to result from reduced temperature, rather than increased shear force. The failure of this study to separate the temperature variable properly from the pressure and shear force variables means that an authoritative comment on the effects of shear force and stagnation pressure on surface oxide species (friable solids or melts) is not possible. It might have been possible to separate these variables using samples with higher thermal resistance. Alternatively, using gas jets in combination with laser heating may have yielded an orthogonal variable testing environment that allowed the independent analysis of the shear and static pressure effects, subsequently potentially permitting greater insight.

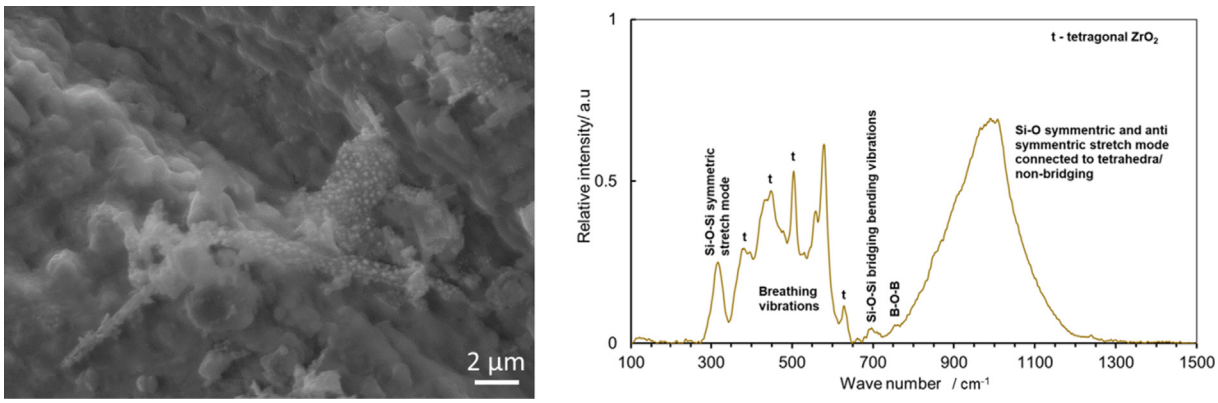

Fig. 13. A high magnification SEM image of the 30° test condition showing nano-ZrO_2 grains embedded in a glassy matrix. The distinct peaks for these phases are shown in the accompanying Raman spectrogram.

The fact that the 90° sample lost most mass but was most oxidised, indicates the importance of the static pressure; the 10° or 30° samples had comparatively low static pressures. While the three variables – temperature, static pressure and shear force – were not fully separated in this study, the results for 90° do indicate that the highest-pressure sample experienced most mass loss. However, these were also the only samples which produced a molten phase during testing – it is possible this phase change resulted in a far more easily displaced/vaporisable component. The mass loss may have resulted from volatilised ZrO_2 or SiO. The reducing trend in $\Delta m/\Delta t$ as the angle of attack was increased was mirrored by the increase in pressure. This highlights that, for a material that did not produce a melt at most angles, the vastly heightened static pressure was more likely responsible for material removal than the shear forces. In essence, more oxide was formed at high angles of attack and correspondingly there was greater pressure-assisted denudation in addition to higher peak temperatures. There is also the possibility that, as was found by Kovácová et al [40], the oxidation protection endowed by Y_2O_3 is most useful at lower temperatures when compared to ZrB_2-SiC alone. The higher temperatures could result simply in poorer oxidation performance. However, unlike Kovácová et al's phase analysis, the XRD results in this study, Fig. 11, do not indicate a loss of the stabilised ZrO_2 phase (and therefore Y_2O_3 content) as they had found for oxidation trials at 1650 °C. The reason for this discrepancy is unknown.

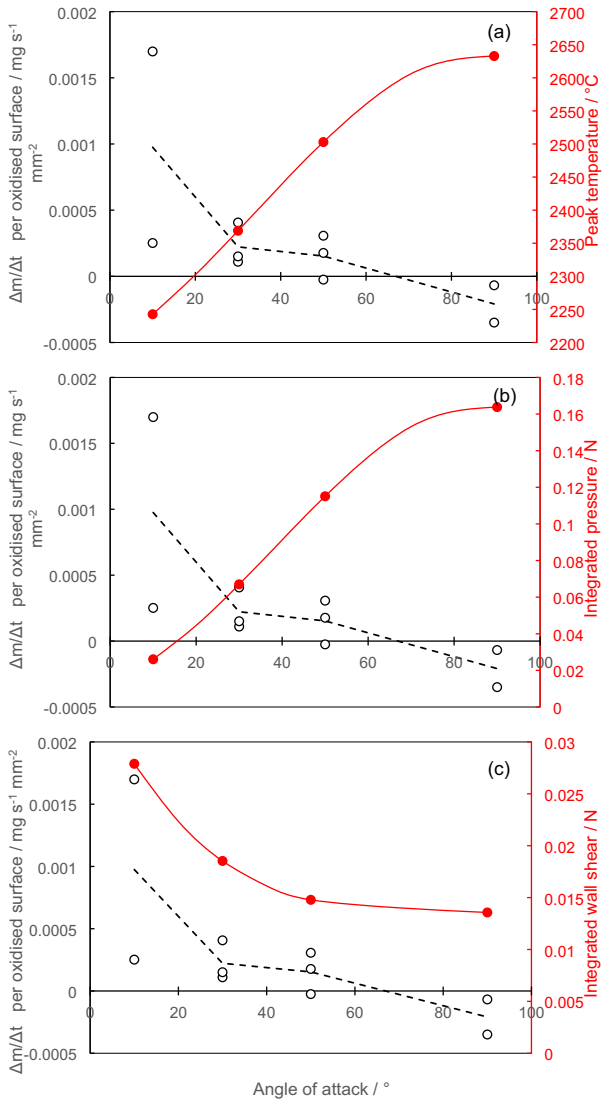

Fig. 14. The correlation of the specific $\Delta m/\Delta t$ with the (a) peak temperature measured and the fluid dynamics calculation outputs, (b) integrated pressure and (c) integrated wall shear. The black trendline tracks the average value, whereas the red trendline is merely a guide.

5. Conclusion

The same torch test distance and gas flow rate were used to provide several ablation environments for a UHTCMC material by the variation of the ablation angle of attack from 90° (perpendicular to the surface) down to 10°.

Experimentally, it was found that smaller angles of attack induced lower surface temperatures, and a higher $\Delta m/\Delta t$ per unit of damaged surface. This correlated microstructurally with the formation of a rough, asperity-dense surface that did not develop a melt during testing. These samples showed a lower extent of oxidation morphologically and a higher mass gain relative to the 90° samples. This suggested that the increased amount of oxide, volumetrically denser, was offset by increasing material loss at more direct (i.e. closer to 90°) angles of attack.

To corroborate this, rudimentary fluid dynamics calculations were performed which indicated higher static pressure across the sample surface in the cases of direct angles of attack, which, in turn, corresponded with the reduced specific $\Delta m/\Delta t$. This analysis was rudimentary in the sense that the temperatures, viscosities and surface dynamics were not taken into account and the simulation was steady-state (not time resolved), hence the specific values produced were only relative measures.

The value of this work is that it has revealed another mode for which material response may be probed via OAT testing; a particularly high-shear, low temperature and pressure regime. The latter environment may be expected downwind of stagnation points in many components relevant in the aerodynamic environment. Angled testing can mirror certain aspects of this and demonstrate not only the different material responses but also provide information on the protection mechanisms that are relevant under the different conditions. This further enhances the cost-effectiveness of OAT set-ups as rapid material screening tools. Functionally graded materials can be designed specifically to match the changing thermal/oxidative gradients as found from systems scale modelling, and the modified OAT test environment as elucidated here may provide such a gradient to better screen the performance of such materials at early stages of production and provide data for design considerations. Secondly, the use of glancing angle testing is far more appropriate an environment, with more representative aerodynamic aspects, for components downwind of leading edges or through apertures or flow channels. In such cases, the heating behaviour and aerothermal heating mechanisms provided by oblique angle of attack OAT testing may provide a more direct method for material screening.

CRediT authorship contribution statement

B. Baker: Conceptualization, Methodology, Investigation, Writing – original draft. **V. Venkatachalam:** Conceptualization, Investigation, Writing – review & editing. **L. Zoli:** Investigation, Writing – review & editing. **A. Vinci:** Investigation, Writing – review & editing. **S. Failla:** Investigation. **D. Sciti:** Funding acquisition. **J. Binner:** Writing – review & editing, Supervision.

Declaration of Competing Interest

The authors declare that they have no known competing financial interests or personal relationships that could have appeared to influence the work reported in this paper.

Acknowledgements

This work has received funding from the European Union's Horizon 2020 "Research and innovation programme" under grant agreement No. 685594 (C3HARME).

Data availability statement

The raw and processed data required to reproduce these findings are available to download from DOI: 10.17632/9ch7z4kt9j.1.

Appendix A. Supplementary material

Supplementary data to this article can be found online at https://doi.org/10.1016/j.matdes.2021.110199.

References

[1] D.M. Van Wie, D.G. Drewry Jr., D.E. King, C.M. Hudson, The hypersonic environment: Required operating conditions and design challenges, J. Mater. Sci. 39 (19) (2004) 5915–5924, https://doi.org/10.1023/B:JMSC.0000041688.68135.8b.
[2] L.V. Kravchuk, K.P. Buiskikh, I.A. Gusarova, A.M. Potapov, N.N. Feofentov, Methods for the Simulation of the Aerodynamic Heating Conditions of the Structural Elements of Space Shuttles, Strength Mater. 50 (4) (2018) 565–574, https://doi.org/10.1007/s11223-018-0002-x.
[3] E.P. Simonenko, D.V. Sevast'yanov, N.P. Simonenko, V.G. Sevast'yanov, N.T. Kuznetsov, Promising ultra-high-temperature ceramic materials for aerospace applications, Russ. J. Inorg. Chem. 58 (14) (2013) 1669–1693, https://doi.org/10.1134/S0036023613140039.
[4] S. Tang, C. Hu, Design, Preparation and Properties of Carbon Fiber Reinforced Ultra-High Temperature Ceramic Composites for Aerospace Applications: A Review, J. Mater. Sci. Technol. 33 (2) (2017) 117–130, https://doi.org/10.1016/j.jmst.2016.08.004.
[5] W.G. Fahrenholtz, G.E. Hilmas, Ultra-high temperature ceramics: Materials for extreme environments, Scr. Mater. 129 (2017) 94–99, https://doi.org/10.1016/j.scriptamat.2016.10.018.
[6] L. Li, Y. Wang, L. Cheng, L. Zhang, Preparation and properties of 2D C/SiC–ZrB2–TaC composites, Ceram. Int. 37 (3) (2011) 891–896, https://doi.org/10.1016/j.ceramint.2010.10.033.
[7] P. Sarin, P.E. Driemeyer, R.P. Haggerty, D.-K. Kim, J.L. Bell, Z.D. Apostolov, W.M. Kriven, In situ studies of oxidation of ZrB2 and ZrB2–SiC composites at high temperatures, J. Eur. Ceram. Soc. 30 (11) (2010) 2375–2386, https://doi.org/10.1016/j.jeurceramsoc.2010.03.009.
[8] A.K. Kuriakose, J.L. Margrave, The Oxidation Kinetics of Zirconium Diboride and Zirconium Carbide at High Temperatures, J. Electrochem. Soc. 111 (1964) 827–831, https://doi.org/10.1149/1.2426263.
[9] A. Vinci, L. Zoli, D. Sciti, J. Watts, G.E. Hilmas, W.G. Fahrenholtz, Influence of fibre content on the strength of carbon fibre reinforced HfC/SiC composites up to 2100 °C, J. Eur. Ceram. Soc. 39 (13) (2019) 3594–3603, https://doi.org/10.1016/j.jeurceramsoc.2019.04.049.
[10] X. Feng, X. Wang, Y. Liu, W. Tian, M. Zhang, X. Jian, L. Yin, L. Zhang, J. Xie, L. Deng, Pursuing enhanced oxidation resistance of ZrB2 ceramics by SiC and WC co-doping, J. Eur. Ceram. Soc. 38 (16) (2018) 5311–5318, https://doi.org/10.1016/j.jeurceramsoc.2018.07.041.
[11] K. Gürcan, E. Ayas, In-situ synthesis and densification of HfB2 ceramics by the spark plasma sintering technique, Ceram. Int. 43 (4) (2017) 3547–3555, https://doi.org/10.1016/j.ceramint.2016.11.164.
[12] L. Silvestroni, S. Failla, I. Neshpor, O. Grigoriev, Method to improve the oxidation resistance of ZrB2-based ceramics for reusable space systems, J. Eur. Ceram. Soc. 38 (6) (2018) 2467–2476, https://doi.org/10.1016/j.jeurceramsoc.2018.01.025.
[13] R. Inoue, Y. Arai, Y. Kubota, Y. Kogo, K. Goto, Oxidation of ZrB2 and its composites: a review, J. Mater. Sci. 53 (21) (2018) 14885–14906, https://doi.org/10.1007/s10853-018-2601-0.
[14] J. Binner, M. Porter, B. Baker, J.i. Zou, V. Venkatachalam, V.R. Diaz, A. D'Angio, P. Ramanujam, T. Zhang, T.S.R.C. Murthy, Selection, processing, properties and applications of ultra-high temperature ceramic matrix composites, UHTCMCs – a review, Int. Mater. Rev. 65 (7) (2020) 389–444, https://doi.org/10.1080/09506608.2019.1652006.
[15] E. Eakins, D.D. Jayaseelan, W.E. Lee, Toward Oxidation-Resistant ZrB2-SiC Ultra High Temperature Ceramics, Metall. Mater. Trans. A. 42 (4) (2011) 878–887, https://doi.org/10.1007/s11661-010-0540-8.
[16] X. Yao, H. Li, Y. Zhang, H. Wu, X. Qiang, A SiC–Si–ZrB2 multiphase oxidation protective ceramic coating for SiC-coated carbon/carbon composites, Ceram. Int. 38 (3) (2012) 2095–2100, https://doi.org/10.1016/j.ceramint.2011.10.047.
[17] R. Savino, M. De Stefano Fumo, D. Paterna, A. Di Maso, F. Monteverde, Arc-jet testing of ultra-high-temperature-ceramics, Aerosp. Sci. Technol. 14 (3) (2010) 178–187, https://doi.org/10.1016/j.ast.2009.12.004.
[18] C. Carney, D. King, M. De Stefano Fumo, C. Purpura, E. Trifoni, A. Martucci, B. Larson, T. Parthasarathy, M. Cinibulk, G. Marino, Oxidation response of a SiCf/SiC CMC with a HfB2-based coating in an arc jet test, Adv. Appl. Ceram. 117 (sup1) (2018) s19–s25, https://doi.org/10.1080/17436753.2018.1509174.
[19] A. Vinci, T. Reimer, L. Zoli, D. Sciti, Influence of pressure on the oxidation resistance of carbon fiber reinforced ZrB2/SiC composites at 2000 and 2200 °C, Corros. Sci. 184 (2021) 109377, https://doi.org/10.1016/j.corsci.2021.109377.
[20] V.V. Kurbatkina, E.I. Patsera, E.A. Levashov, A.N. Timofeev, Self-propagating high-temperature synthesis of refractory boride ceramics (Zr, Ta)B2 with superior properties, J. Eur. Ceram. Soc. 38 (4) (2018) 1118–1127, https://doi.org/10.1016/j.jeurceramsoc.2017.12.031.
[21] A. Vinci, L. Zoli, D. Sciti, Influence of SiC content on the oxidation of carbon fibre reinforced ZrB2/SiC composites at 1500 and 1650 °C in air, J. Eur. Ceram. Soc. 38 (11) (2018) 3767–3776, https://doi.org/10.1016/j.jeurceramsoc.2018.04.064.
[22] A. Vinci, L. Zoli, P. Galizia, D. Sciti, Influence of Y2O3 addition on the mechanical and oxidation behaviour of carbon fibre reinforced ZrB2/SiC composites, J. Eur. Ceram. Soc. 40 (15) (2020) 5067–5075, https://doi.org/10.1016/j.jeurceramsoc.2020.06.043.
[23] A. Paul, S. Venugopal, J.G.P. Binner, B. Vaidhyanathan, A.C.J. Heaton, P.M. Brown, UHTC–carbon fibre composites: Preparation, oxyacetylene torch testing and characterisation, J. Eur. Ceram. Soc. 33 (2) (2013) 423–432, https://doi.org/10.1016/j.jeurceramsoc.2012.08.018.
[24] Y. Liu, Q. Fu, J. Zhang, L.u. Li, L. Zhuang, Erosion resistance of C/C-SiC-ZrB2 composites exposed to oxyacetylene torch, J. Eur. Ceram. Soc. 36 (15) (2016) 3815–3821, https://doi.org/10.1016/j.jeurceramsoc.2016.04.007.
[25] C. Yan, R. Liu, B. Zha, C. Zhang, Fabrication and properties of 3-dimensional 4-directional Cf/HfC-SiC composites by precursor impregnation and pyrolysis process, J. Alloys Compd. 739 (2018) 955–960, https://doi.org/10.1016/j.jallcom.2017.12.059.
[26] L. Silvestroni, A. Vinci, S. Failla, L. Zoli, V. Rubio, J. Binner, D. Sciti, Ablation behaviour of ultra-high temperature ceramic matrix composites: Role of MeSi2 addition, J. Eur. Ceram. Soc. 39 (9) (2019) 2771–2781, https://doi.org/10.1016/j.jeurceramsoc.2019.03.031.
[27] A. Paul, J.G.P. Binner, B. Vaidhyanathan, A.C.J. Heaton, P.M. Brown, Heat flux mapping of oxyacetylene flames and their use to characterise Cf-HfB2

composites, Adv. Appl. Ceram. 115 (3) (2016) 158–165, https://doi.org/10.1080/17436753.2015.1104050.
[28] J. Marschall, D.G. Fletcher, High-enthalpy test environments, flow modeling and in situ diagnostics for characterizing ultra-high temperature ceramics, J. Eur. Ceram. Soc. 30 (11) (2010) 2323–2336, https://doi.org/10.1016/j.jeurceramsoc.2010.01.010.
[29] C. Ni, K. Li, L. Liu, H. Li, Q. Fu, L. Guo, N. Liu, Ablation mechanism of SiC coated C/C composites at 0° angle in two flame conditions under an oxyacetylene flame, Corros. Sci. 84 (2014) 1–10, https://doi.org/10.1016/j.corsci.2014.03.009.
[30] A. Gao, C. Zhao, S. Luo, Y. Tong, L. Xu, Correlation between graphite crystallite distribution morphology and the mechanical properties of carbon fiber during heat treatment, Mater. Lett. 65 (23-24) (2011) 3444–3446, https://doi.org/10.1016/j.matlet.2011.07.057.
[31] J. Crafton, C. Carter, G. Elliott, J. Sullivan, The impingement of sonic and subsonic jets onto a flat plate at inclined angles, Exp. Fluids. 41 (5) (2006) 699–710, https://doi.org/10.1007/s00348-006-0192-z.
[32] D. Sciti, L. Zoli, L. Silvestroni, A. Cecere, G.D. Di Martino, R. Savino, Design, fabrication and high velocity oxy-fuel torch tests of a Cf-ZrB2- fiber nozzle to evaluate its potential in rocket motors, Mater. Des. 109 (2016) 709–717, https://doi.org/10.1016/j.matdes.2016.07.090.
[33] L. Zoli, A. Vinci, P. Galizia, C.F. Gutièrrez-Gonzalez, S. Rivera, D. Sciti, Is spark plasma sintering suitable for the densification of continuous carbon fibre - UHTCMCs?, J Eur. Ceram. Soc. 40 (7) (2020) 2597–2603, https://doi.org/10.1016/j.jeurceramsoc.2019.12.004.
[34] H. Ma, Q. Miao, W. Liang, Y. Liu, H. Lin, H. Ma, S. Zuo, L. Xue, High temperature oxidation resistance of Y2O3 modified ZrB2-SiC coating for carbon/carbon composites, Ceram. Int. 47 (5) (2021) 6728–6735, https://doi.org/10.1016/j.ceramint.2020.11.015.
[35] M. Okkerse, C.R. Kleijn, H.E.A. van den Akker, M.H.J.M. de Croon, G.B. Marin, Two-dimensional simulation of an oxy-acetylene torch diamond reactor with a detailed gas-phase and surface mechanism, J. Appl. Phys. 88 (2000) 4417–4428, https://doi.org/10.1063/1.1309052.
[36] M.H. Weik, Lambert's cosine law BT - Computer Science and Communications Dictionary, in: M.H. Weik (Ed.), Springer US, Boston, MA, 2001: p. 868. https://doi.org/10.1007/1-4020-0613-6_9901.
[37] N. Jacobson, Thermodynamic properties of some metal oxide-zirconia systems, NASA Technical Memorandum 102351 (1989).
[38] T. Kondo, H. Muta, K. Kurosaki, F. Kargl, A. Yamaji, M. Furuya, Y. Ohishi, Density and viscosity of liquid ZrO2 measured by aerodynamic levitation technique, Heliyon 5 (7) (2019) e02049, https://doi.org/10.1016/j.heliyon.2019.e02049.
[39] P. Barreiro, P. Rey, A. Souto, F. Guitián, Porous stabilized zirconia coatings on zircon using volatility diagrams, J. Eur. Ceram. Soc. 29 (4) (2009) 653–659, https://doi.org/10.1016/j.jeurceramsoc.2008.07.018.
[40] L. Silvestroni, C. Melandri, V. Venkatachalam, J. Binner, D. Sciti, Merging toughness and oxidation resistance in a light ZrB2 composite, Mater. Des. 183 (2019) 108078, https://doi.org/10.1016/j.matdes.2019.108078.